nature materials

Article

https://doi.org/10.1038/s41563-023-01611-3

Fibre-infused gel scaffolds guide cardiomyocyte alignment in 3D-printed ventricles

Received: 6 June 2022

Accepted: 19 June 2023

Published online: 27 July 2023

Check for updates

Suji Choi[1], Keel Yong Lee[1,2], Sean L. Kim[1], Luke A. MacQueen[1], Huibin Chang[1], John F. Zimmerman[1], Qianru Jin[1], Michael M. Peters[1], Herdeline Ann M. Ardoña[1,3], Xujie Liu[4,5], Ann-Caroline Heiler[6,7,8], Rudy Gabardi[1], Collin Richardson[1], William T. Pu[4,9], Andreas R. Bausch[6,7,8,10] & Kevin Kit Parker[1,9,11] ✉

Hydrogels are attractive materials for tissue engineering, but efforts to date have shown limited ability to produce the microstructural features necessary to promote cellular self-organization into hierarchical three-dimensional (3D) organ models. Here we develop a hydrogel ink containing prefabricated gelatin fibres to print 3D organ-level scaffolds that recapitulate the intra- and intercellular organization of the heart. The addition of prefabricated gelatin fibres to hydrogels enables the tailoring of the ink rheology, allowing for a controlled sol–gel transition to achieve precise printing of free-standing 3D structures without additional supporting materials. Shear-induced alignment of fibres during ink extrusion provides microscale geometric cues that promote the self-organization of cultured human cardiomyocytes into anisotropic muscular tissues in vitro. The resulting 3D-printed ventricle in vitro model exhibited biomimetic anisotropic electrophysiological and contractile properties.

The intra- and intercellular organization within cardiac tissues helps facilitate coordinated electromechanical coupling and efficient muscle contraction in the heart. To achieve these organized structures, extracellular matrix (ECM) proteins act as topological and biochemical cues for the cells, which are crucial for tissue development[1,2]. This is particularly important in the heart, where the hierarchical organization of cardiac tissues[3] is needed to regulate the spatiotemporal dynamics of excitation–contraction coupling, resulting in the cardiac cycle[4,5]. However, recreating the structure–function relationships of the heart in vitro represents a substantial challenge, requiring control over tissue self-organization both at the cellular scale and at the macroscopic organ level.

In an effort to replicate cardiac cellular organization, researchers have engineered biopolymers and hydrogels through microcontact printing[6–10], photolithography[11], directional freeze drying[12], fibre spinning[13–15] and microphysiological chip fabrication[4,16–19].

[1]Disease Biophysics Group, John A. Paulson School of Engineering and Applied Sciences, Harvard University, Boston, MA, USA. [2]Department of Integrative Bioscience and Biotechnology, Sejong University, Seoul, Republic of Korea. [3]Department of Chemical and Biomolecular Engineering, Samueli School of Engineering, University of California, Irvine, CA, USA. [4]Department of Cardiology, Boston Children's Hospital, Boston, MA, USA. [5]Fuwai Hospital Chinese Academy of Medical Sciences, Shenzhen, China. [6]Department of Bioscience, TUM School of Natural Sciences, Technische Universität München, Garching, Germany. [7]Center for Functional Protein Assemblies, Technische Universität München, Garching, Germany. [8]Center for Organoid Systems (COS), Technische Universität München, Garching, Germany. [9]Harvard Stem Cell Institute, Harvard University, Cambridge, MA, USA. [10]Max Planck School Matter to Life, Max Planck Schools, Heidelberg, Germany. [11]Wyss Institute for Biologically Inspired Engineering, Harvard University, Boston, MA, USA. ✉e-mail: kkparker@g.harvard.edu

https://doi.org/10.1038/s41563-023-01611-3

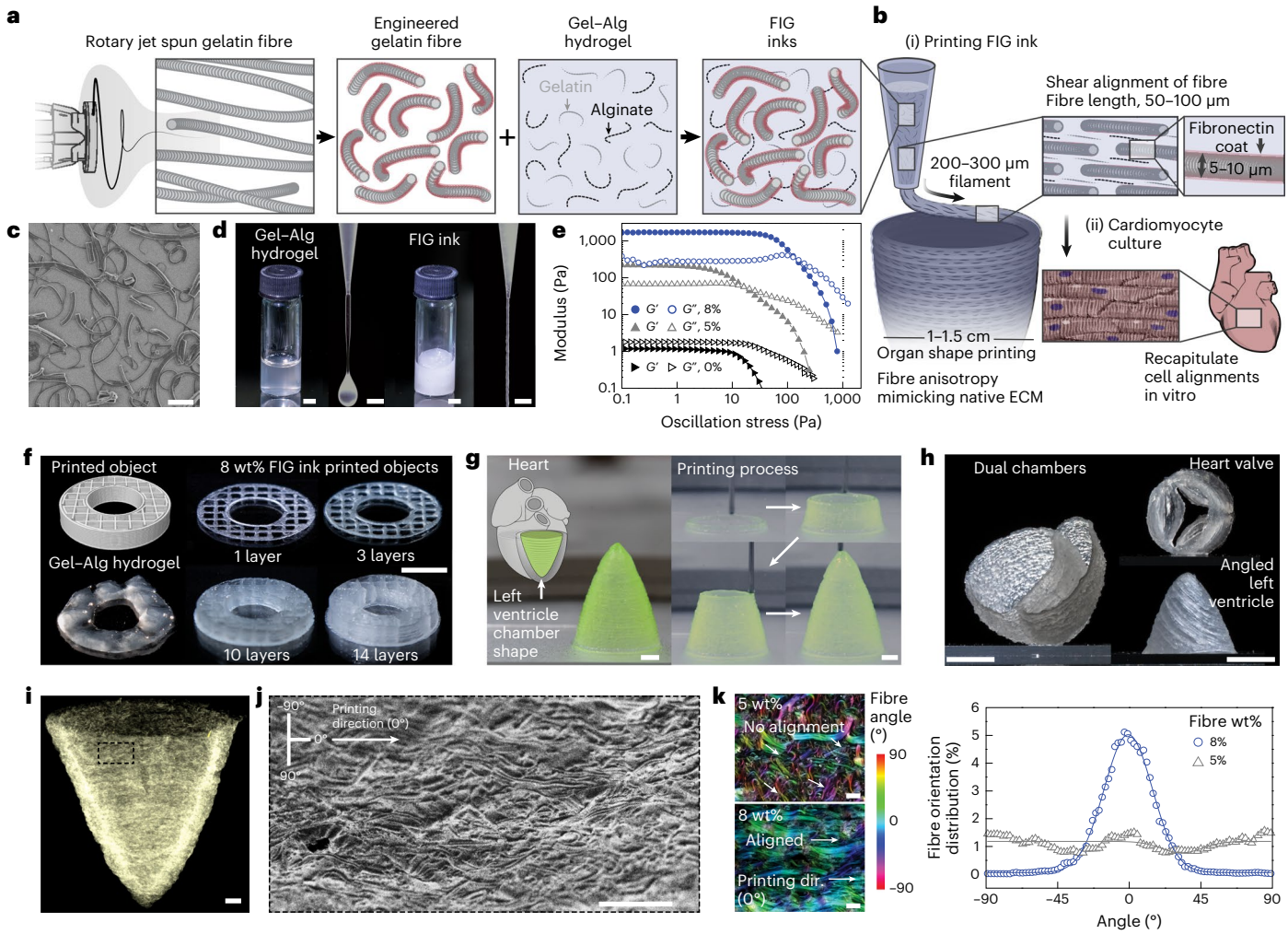

Fig. 1 | Development of gelatin FIG inks for free-standing 3D-printed tissue scaffolds with cellular alignment cues. a,**b**, Schematic illustration of FIG ink components. As fragmented gelatin fibres are combined with Gel–Alg hydrogels (red, fibronectin; **a**), the ink viscosity increases and displays a solid-like behaviour, which allows the 3D printing of ventricle scaffolds with hierarchical structure (**b**). **b**, Fibre alignment that occurs under shear stress (τ) during 3D printing leads to native ECM anisotropic structural features in 3D scaffolds, promoting tissue alignment and organization to recapitulate in vivo heart muscle. **c**, A scanning electron microscopy image showing truncated gelatin fibres. Scale bar, 100 μm. **d**, Comparison of Gel–Alg ink (0 wt% fibre, left panel) or FIG ink (8 wt% fibre, right panel). The Gel–Alg hydrogel has a low-viscosity-liquid-like behaviour (left). FIG inks behave solid-like at rest and extrude in a continuous stream (right). Scale bars, 2 mm. **e**, Oscillation stress sweep test to measure storage (G') and loss (G'') modulus values, showing a concentration-dependent and strain-dependent shear thinning behaviour and sol–gel transition. **f**, A 3D donut shape with rectilinear infill pattern with increasing number of stacking layers, showing the high shape retention of using FIG inks. Scale bar, 5 mm. **g**, A cone-shaped model of the self-supporting inverted left ventricle printed in the circumferential direction. Scale bars, 2 mm. **h**, Self-supportive dual ventricle chambers and a heart valve printed in the circumferential direction and an angled left ventricle printed in the diagonal (30°) tilted direction. Scale bars, 5 mm. **i**, A microcomputed tomography image of the 3D-printed ventricle scaffold after critical-point drying, showing the fibre structure in the 3D-printed geometry. Scale bar, 1 mm. **j**, A scanning electron microscopy image of the 3D-printed ventricle scaffold showing fibre alignments in the printing direction. Scale bar, 200 μm. **k**, Analysis of fibre alignment from confocal images of the 3D-printed ventricle FIG scaffolds with 5 and 8 wt% fibres, and corresponding fibre orientation angular distribution graph; 0° indicates the printing direction (dir.). Scale bars, 100 μm.

These methods are, however, limited in their ability to produce tissues on complex geometries that fully replicate cardiac function. Specifically, to build organ models that mimic the three-dimensional (3D) geometry requires additive manufacturing strategies[15,20]. Particularly, 3D printing has been increasingly used for engineering tissue models to enable the facile design and editing of a 3D structure prior to printing, and the fabrication of complex 3D structures with a flexible formulation of biomaterial inks[21–23]. To this end, considerable efforts have been made in developing hydrogel-based inks or printing techniques to enhance 3D stability and shape fidelity, such as printing multimaterial inks with a combined nozzle system[24,25], printing photo-crosslinkable hydrogels[17,26,27], adding viscosifiers[28–30] or printing in sacrificial supporting materials[31–33]. However, these efforts provide limited control over tissue self-organization and alignment. As a result, bridging the length scales from the micrometre and nanometre scales to the centimetre scale to induce both intra- and intercellular organization within engineered heart models remains a major challenge in the 3D printing of functional organs and tissues[32,34,35].

We reasoned that printing 3D scaffolds containing prefabricated microscale fibres would provide self-supportive scaffolds for cardiomyocytes to self-organize to form a cardiac chamber. Inspired by the ECM networks of the heart, we designed our ink by infusing gelatin fibres into a gelatin and alginate (Gel–Alg) hydrogel matrix (Fig. 1a). In contrast to cellulose nanofibres and carbon nanotubes, previously used in inks[36–38], fibronectin-coated gelatin fibres contain arginine–glycine–aspartic acid (RGD) peptide binding domains that promote matrix–cell

adhesion through integrins[39]. Furthermore, incorporating fibres into the hydrogel modifies the ink rheology, allowing one to create accurate and complex 3D scaffolds without any supporting structures or materials. We hypothesized that by incorporating both topological and chemical cues in the form of aligned gelatin microfibres, 3D ventricle scaffolds printed in this manner would promote the self-organization of cardiomyocytes into anisotropic muscle tissues (Fig. 1b).

Results

Printed 3D hydrogel scaffolds provide microscale anisotropy

We fabricated fibre-infused gel (FIG) inks for printing 3D scaffolds consisting of gelatin fibres (Fig. 1c) and Gel–Alg hydrogel (Fig. 1d and Supplementary Fig. 1a). Gelatin fibres produced by rotary jet spinning (Supplementary Fig. 1b)[14,15] were truncated by ultrasonication to a length of 85.9 ± 2.53 µm with a diameter of 4.20 ± 0.23 µm (mean ± standard error of the mean (s.e.m.)), reducing the variance in length and enabling passage through a printing nozzle with a diameter of 200 µm (Supplementary Fig. 1c,d). Afterward, we chemically crosslinked the fibres with *N*-(3-dimethylaminopropyl)-*N*′-ethylcarbodiimidehydrochloride *N*-hydroxysuccinimide (EDC/NHS) and fibronectin (Supplementary Fig. 1e). Unlike Gel–Alg hydrogels where 3D printing is limited due to their fluidity, incorporating 8 wt% prefabricated gelatin fibres into Gel–Alg hydrogels rendered the hydrogels into a predominantly elastic gel (8 wt% fibre, 2.4 wt% gelatin, 2.4% alginate in phosphate buffered saline (PBS); Fig. 1d–f and Supplementary Fig. 2a–d). During printing, shear stresses in the nozzle were sufficient to turn the elastic FIG ink into a liquid, and its elastic stability was restored upon extrusion (Supplementary Fig. 2e). These nonlinear rheological properties allow for the continuous extrusion of FIG inks with minimal post-extrusion swelling and spreading (Fig. 1d,e and Supplementary Fig. 3) and enable the printing of layered structures for increasingly complex geometries without sacrificial layers or a sacrificial bath as supporting structures (Fig. 1f). This allowed us to print self-supportive hollow 3D structures such as a cardiac ventricle with a broad range of design parameters, reproducibility and accuracy (Fig. 1g, Supplementary Fig. 4a,b and Supplementary Video 1). More complex structures, such as heart valves, dual-chambered hearts and left ventricles with varying angular orientations, could also be printed using FIG inks (Fig. 1h and Supplementary Fig. 4c,d). The high elastic modulus of gel-like FIG inks provided sufficient gel stability to print self-supportive walls with thicknesses ranging between 200 µm and 350 µm without the need for scaffolds or sacrificial baths (Supplementary Fig. 2a–g and the section 'Rheology of FIG inks' in the Supplementary Information).

Inducing cardiac muscle cells to recapitulate the structure–function relationships of heart muscle requires structural anisotropy and biochemical guidance cues with micrometre-scale precision. To achieve this, we exploited the shear thinning property of FIG inks (Supplementary Fig. 2h,i), which is not only essential for printing, but also for inducing fibre alignment along the direction of printing[40]. This allowed the formation of aligned-fibre-embedded scaffolds, which can be used to direct cardiomyocyte alignment. Following this process, shear-induced fibre alignment on the micrometre scale was achieved across the entire length scale of the printed structure (Fig. 1i,j). Alignment of the incorporated fibres was well-maintained post extrusion due to the gel stability of the FIG inks (Fig. 1k and Supplementary Fig. 5), which was further enhanced by lowering the printing bed temperature to 6 °C compared to printing at room temperature (Supplementary Fig. 2f). By the ionic crosslinking of alginate (1 wt% calcium chloride) and enzymatic crosslinking of gelatin (~8 wt% microbial transglutaminase), the printed scaffolds and their microscale architecture remained intact in water (Supplementary Fig. 4b). The resulting printed scaffolds had a resolution closer to the fibre diameter (~5 µm) and acted as geometric cues for cell alignment despite the printing resolution being limited by the nozzle diameter (200–300 µm).

Fibre-infused gel scaffolds potentiate cellular alignment

To evaluate the ability of FIG printed scaffolds to potentiate the intra- and intercellular organization of cardiomyocytes, myofibrillar organization and alignment, we first seeded neonatal rat ventricular cardiomyocytes (NRVMs) on printed two-dimensional (2D) FIG scaffolds (8 wt% fibre, 2.4 wt% gelatin and 2.4 wt% alginate; Supplementary Fig. 6a). This resulted in the formation of highly aligned cardiac tissues (Fig. 2a,b and Supplementary Fig. 6b), which retained comparable cell viabilities relative to pleomorphic culture conditions (Supplementary Fig. 7). We then measured the degree of structural tissue anisotropy by computing the orientational order parameter (OOP)[41], which quantifies sarcomeric α-actinin and cytoskeletal actin filament (F-actin) alignment, representative of intra- and intercellular organization (Fig. 2c and Supplementary Fig. 6c). In physiologically healthy cardiac tissues, cytoskeletal structures including sarcomeres[42,43] and actin filaments[44,45] are highly aligned, with OOP values close to unity. Here, both sarcomeric and F-actin OOP values were significantly higher for tissues on FIG scaffolds (0.578 ± 0.060 for α-actinin, 0.657 ± 0.021 for F-actin, mean ± s.e.m., $n = 5$) in comparison to control Gel–Alg scaffolds that contain a similar chemical composition to FIG scaffolds without microscale topologies (4 wt% gelatin and 4 wt% alginate, 0.245 ± 0.033 for α-actinin, 0.314 ± 0.052 for F-actin, mean ± s.e.m., $n = 5$). Consequently, the prestress generated by intra- and intercellular cytoskeletal structures determined the nuclear elongation and orientation[46,47]. Nuclei were elongated on FIG scaffolds with a mean eccentricity ratio (the length of the major axis to the length of the minor axis) of 2.37 ± 0.17 compared to nuclei on the control Gel–Alg scaffolds, which remained relatively round (eccentricity ratio = 1.40 ± 0.02, mean ± s.e.m.; Fig. 2d,e). The nuclear orientation of NRVMs on FIG scaffolds also aligned along the printing direction (0°) in contrast to those on the control Gel–Alg scaffolds, which showed no specific orientation (Fig. 2d,f and Supplementary Fig. 6d).

Cardiac tissues on FIG recapitulate functional anisotropy

The goal of engineering cardiomyocyte alignment and organization is to better replicate the spatiotemporal excitation and contraction dynamics of the heart in vitro. To test the ability of FIGs to induce cardiomyocytes to self-organize along the fibre structures and form a functional syncytium of the heart[5,48], we measured the functional consequence of a cell–cell junction architecture (Supplementary Fig. 6e) and its electrophysiological properties. Cardiac impulses propagate in aligned cardiac tissues approximately two times faster in the longitudinal (V_{long}) than the transverse (V_{trans}) direction ($V_{long}/V_{trans} \approx 2$) due to rapid conduction along the longitudinal axis and intercellular conduction at gap junctions[49]. We used optical mapping to measure the calcium (Ca^{2+}) transient propagation as an indicator of cardiac impulse conduction along the longitudinal and transverse axes relative to the printing direction. We assessed the anisotropic propagation by calculating the longitudinal-to-transverse propagation speed ratio (V_{long}/V_{trans}; Fig. 3a,b). Cardiac tissues on FIG scaffolds using NRVMs and human-induced pluripotent stem-cell-derived cardiomyocytes (hiPSC-CMs; Supplementary Fig. 8a and Supplementary Video 2) exhibited V_{long}/V_{trans} values of 1.67 ± 0.085 and 1.62 ± 0.18, respectively (mean ± s.e.m.; Fig. 3b, Supplementary Figs. 6f,g and 8b and Supplementary Videos 3 and 4). By contrast, NRVM tissues on control scaffolds without fibres exhibited a propagation speed ratio close to unity (0.96 ± 0.067 at day 5; mean ± s.e.m.) indicating their isotropy. Cardiac tissues on FIG scaffolds also propagated Ca^{2+} waves over a 6 cm serpentine pattern, demonstrating robust electrical coupling along the direction of printing (Supplementary Fig. 9 and Supplementary Video 5).

Further, to assess the effect of fibre anisotropy on the contractile patterns in electrically coupled cardiac tissues, we cultured NRVMs on rectangular scaffolds printed in parallel, angled and perpendicular directions (10 mm × 3 mm; Supplementary Fig. 10a–c and Supplementary Video 6). Each FIG orientation resulted in distinct contractile

https://doi.org/10.1038/s41563-023-01611-3

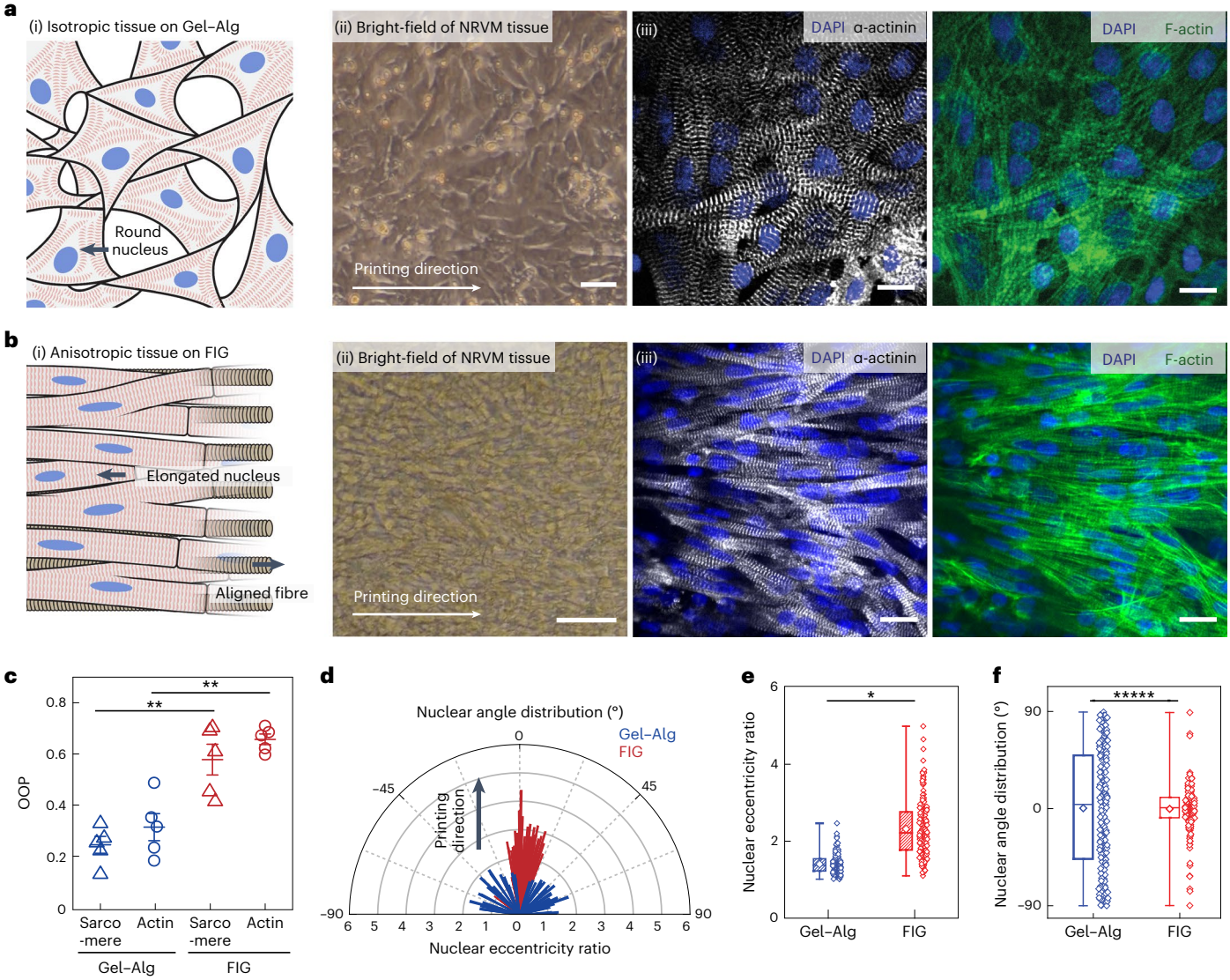

Fig. 2 | Anisotropic intra- and intercellular organization of cardiac tissues cultured on printed FIG scaffolds. a,**b**, Schematic illustrations showing NRVM tissue formation on the 2D-printed Gel–Alg hydrogel (**a**) and FIG (**b**) scaffolds (i), bright-field images of NRVM cultured on each scaffold (ii) and representative immunostained images of nuclei (blue), α-actinin (grey) and F-actin (green; iii). Scale bars, 20 µm. DAPI stain, 4′,6-diamidino-2-phenylindole. **c**, Normalized sarcomeric α-actinin and F-actin alignment with their alignment quantified on a scale of 0 (random) to 1 (aligned) using an OOP. Statistical analysis was performed using a two-tailed Student's *t*-test with unequal variance; $^{**}P = 0.000252$ and 0.00149 for sarcomere and F-actin, respectively. $n = 5$ tissues per scaffold condition. Data are presented as mean values ± s.e.m. **d**, Representative distribution of nuclear shape (line length to eccentricity ratio) and orientation (line angle) with printing direction at 0°. **e**,**f**, Nuclear eccentricity ratio (**e**) and angle (**f**) from −90° to 90° ($n = 203$ and 183 nuclei from three tissues on Gel–Alg and FIG scaffolds, respectively). Statistical analysis was performed using a two-tailed Student's *t*-test with unequal variance, $^{*}P = 0.0295$ (**e**); and a two-sample Kolmogorov–Smirnov test, $^{*****}P = 3.46 \times 10^{-10}$ (**f**); $n = 203$ and 183 nuclei from three independent tissues on Gel–Alg and FIG scaffolds, respectively. In the box plot, the centre diamond, box limits and whiskers indicate the mean, the first and third quartiles and the maximum–minimum, respectively.

patterns, such as rolling, twisting and folding, respectively (Fig. 3c–e). Preferential electromechanical coupling of cardiomyocytes along the printing direction enabled cyclic deformations in response to electrical stimulation (Fig. 3e,f). Alternating alignment directions in one scaffold also showed that cardiomyocyte organization follows the local fibre direction, resulting in corresponding local tissue contractile patterns (Supplementary Fig. 10b). This enables control of local dynamic contractile motions similar to those seen in laminar muscles around the ventricle[50].

As FIG scaffolds can be printed in a highly scalable and reproducible manner, they can also easily be adapted to rapidly fabricate previously published standardized metrics of quantifying cellular contractile force via muscular thin films (MTFs; Supplementary Fig. 10d)[9]. NRVM tissues cultured on FIG MTFs (day 7) displayed average contractile forces of 1,661 ± 209 Pa, which were comparable to NRVMs cultured on polydimethylsiloxane MTFs (1,801 ± 428 Pa; mean ± s.e.m.; Supplementary Fig. 10e,f), showing a response to increased pacing frequencies up to 3 Hz (Supplementary Fig. 10g). In addition, FIG MTFs enabled us to assess the contractility of hiPSC-CM tissues. We found the contractile stress of hiPSC-CM tissues to be 455 ± 130 Pa (mean ± s.e.m.) at day 14 (Supplementary Fig. 10d–f), which was significantly lower than the more mature NRVM tissues.

Engineered 3D ventricle models exhibit cyclic contractility

Given the ability to efficiently control tissue alignment and thus, electromechanical coupling, we questioned whether we could build

https://doi.org/10.1038/s41563-023-01611-3

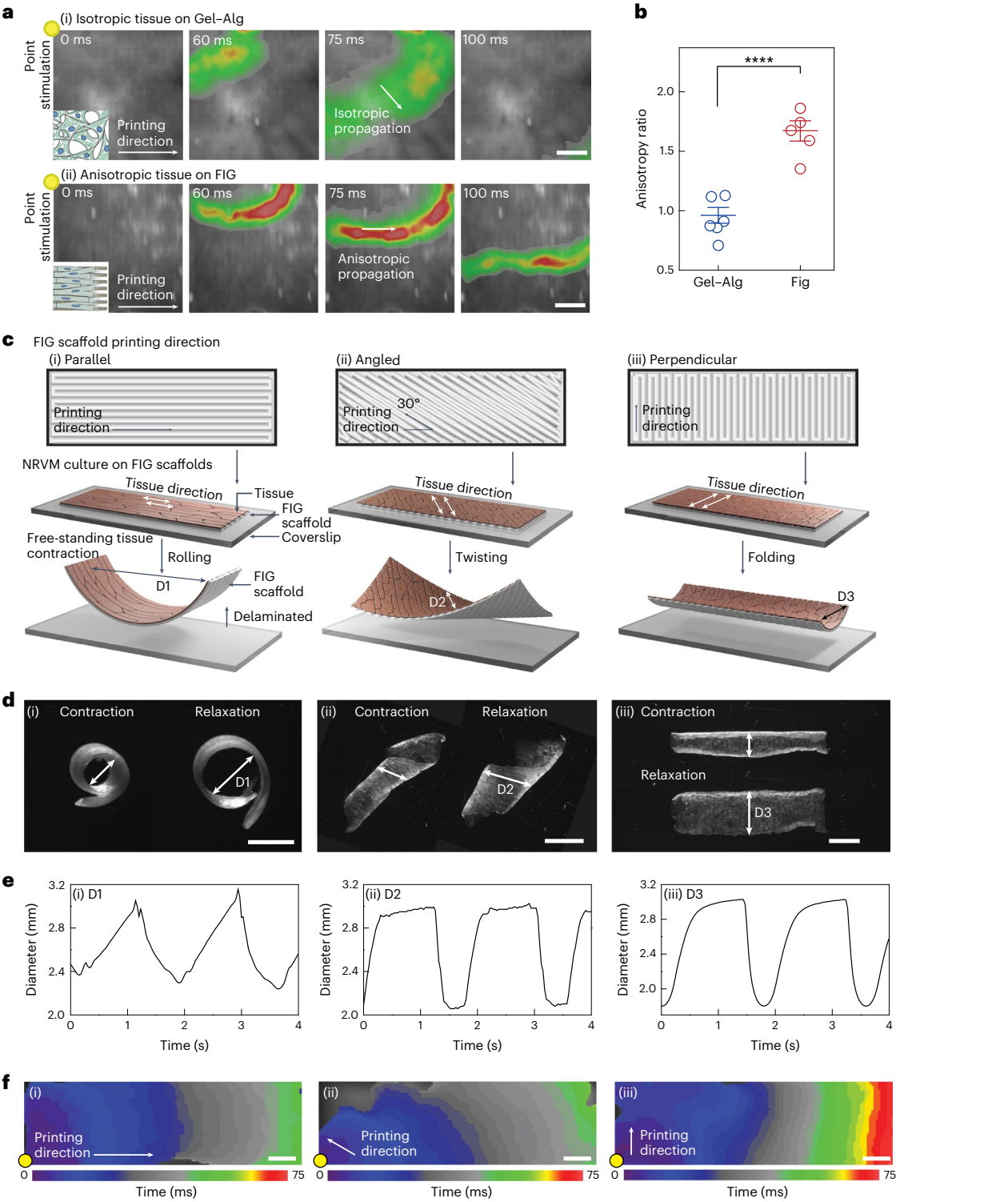

Fig. 3 | Dynamics of electromechanical coupling of multidirectional anisotropic cardiac tissues. a, Representative Ca^{2+} transient propagation images from Ca^{2+} optical mapping of NRVM tissues cultured on Gel–Alg scaffolds (i) and FIG scaffolds (ii), resulting in isotropic (i) and anisotropic (ii) Ca^{2+} propagation, respectively, under 1 Hz point electrical stimulation at the top-left corner (yellow dot). Scale bars, 2 mm. **b**, The anisotropy ratio (V_{long}/V_{trans}) for NRVM tissues on Gel–Alg scaffolds and FIG scaffolds, quantifying anisotropic Ca^{2+} propagation. Statistical analysis was performed using a two-tailed Student's *t*-test with unequal variance; $^{****}P = 0.000174$; $n = 6$ or 5 tissues per scaffold condition. Data are presented as mean values ± s.e.m. **c**,**d**, Schematic illustration (**c**) and microscope images (**d**) of NRVM tissue cultured on rectangular FIG scaffolds printed in a parallel (i), angled (ii) and perpendicular (iii) direction relative to the long side of the scaffold geometry. Delaminated free-standing tissue layers from the coverslip showed different contractile motions: rolling (i), twisting (ii) and bending (iii). Scale bars, 2 mm. **e**, Diameter (D, arrow in **d**) showing how the deformed shape continuously changes in time under 0.5 Hz field electrical stimulation. D1, D2 and D3 represent the different patterns of deformation. **f**, Isochron mapping images demonstrating Ca^{2+} propagation of NRVM tissues on parallel (i), angled (ii) and perpendicular (iii) patterned FIG scaffolds. Point electrical stimulation at 1 Hz (yellow dot) initiates the Ca^{2+} propagation, showing fast propagation in the parallel and angled patterns but slow propagation in the perpendicular pattern throughout the scaffold geometry. Scale bars, 1 mm.

https://doi.org/10.1038/s41563-023-01611-3

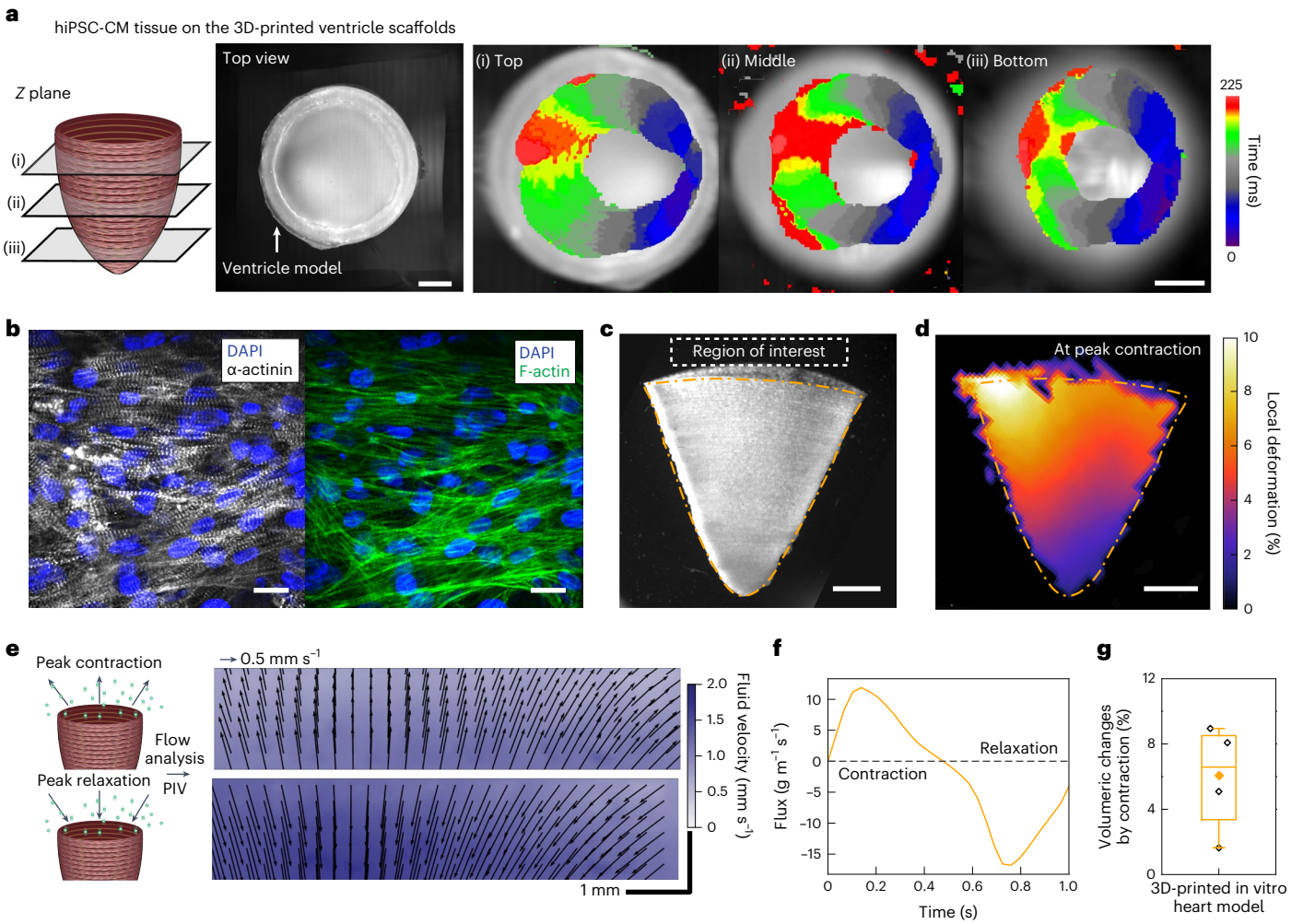

Fig. 4 | Structural, electrophysiological and contractile properties of human-stem-cell-based tissue-engineered 3D ventricle models. a, Spontaneous Ca^{2+} transient propagation on a hiPSC-CM 3D-printed ventricle model (top view), showing anisotropic Ca^{2+} propagation along the printing direction. Scale bars, 2 mm. **b**, Immunostained images of hiPSC-CM tissues cultured in 3D-printed model ventricle scaffolds. Scale bars, 20 µm. **c**, A bright-field image of the tissue-engineered 3D ventricle model after hiPSC-CMs were cultured for 14 days. Scale bar, 2 mm. **d**, Representative deformation map of the 3D hiPSC-CM ventricle model at peak contraction. Scale bar, 2 mm. **e**, Fluid velocity maps at peak contraction (top) and peak relaxation (bottom) analysed by tracking fluorescent bead displacement in a region of interest under 1 Hz electrical field stimulation. **f**, Instantaneous mass flux in a region of interest for a representative ventricle during a complete cycle of contraction and relaxation. **g**, Volumeric changes by contraction of hiPSC-CM 3D ventricle models. $n = 4$ ventricle models. In the box plot, the centre diamond, box limits and whiskers indicate the mean, the first and third quartiles and the maximum–minimum, respectively.

3D ventricle-shaped cardiac tissues in vitro, where the 3D geometry would induce synchronized contractile pumping motions as seen in human hearts. We cultured NRVMs and hiPSC-CMs on a 3D-printed ventricle scaffold (8 wt% fibre, 2.4 wt% gelatin and 2.4 wt% alginate) with circumferential fibre alignment, forming laminar anisotropic cardiac tissues in a 3D ventricular shape (Fig. 4a,b, Supplementary Fig. 11 and Supplementary Videos 7 and 8). The in vitro ventricle models were maintained for 14 days in culture with a spontaneous beat rate of ~0.71 beats per second. This suggested that the scaffolds were durable over ~800,000 mechanical load cycles without visible degradation. Following the point electrical stimulation of the NRVM cultured ventricle models, we observed that Ca^{2+} transient propagations were faster in the transverse direction (the direction of printing) compared to the longitudinal direction (Supplementary Fig. 12a,b and Supplementary Video 9). This confirms that impulse propagation in the 3D-printed ventricle scaffolds also occurred along tissue alignment, which is determined by the printing direction. Similarly, in hiPSC-CM cultured ventricle models, directional Ca^{2+} transient propagations indicated the confluency and synchronization of cardiomyocytes across the 3D-printed ventricle scaffolds (Fig. 4a, Supplementary Fig. 12c and Supplementary Video 10). This led to the synchronized and coordinated contractions of hiPSC-CM cultured ventricle models, which were demonstrated by deformation mapping analysis, measuring the displacement of the in vitro ventricle models (Fig. 4c,d and Supplementary Video 11). To assess the contractile performance of hiPSC-CM ventricle models, we measured the fluid-dynamic output at the basal opening (shown in Fig. 4c, grey box) using particle imaging velocimetry (PIV). The flow of fluorescent microparticles corresponded with the fluid movement out of and into the in vitro ventricle models (Fig. 4e, Supplementary Fig. 12d and Supplementary Video 12). The direction and velocity of particle flow allowed us to estimate the mass flux of the fluid movement during contraction and relaxation (Fig. 4f). We calculated the change in ventricular volume for our hiPSC-CM cultured ventricle models to be 5.94 ± 1.66% ($n = 4$, mean ± s.e.m.; Fig. 4g) between peak contraction and peak relaxation. This was 2–5 and 8–20 times higher than values previously reported (ejection fractions) for NRVM and hiPSC-CM in vitro ventricle models, respectively[13,15,32].

Outlook

We have demonstrated the ability to 3D print tissue-engineered ventricle models with hydrogel-based FIG ink, which simultaneously recapitulates the heart's microstructural ECM architecture and macrostructural organ-level geometry. Here, infused gelatin fibres acted as a rheological modifier in our hydrogel inks, allowing for the printing of complex 3D objects without the use of sacrificial baths. In addition, these fibres also provided biochemical and microstructural cues, which promoted cell adhesion and self-organization into a functional syncytium. Resulting in vitro ventricle models showed cyclic contractile motions of the heart; however, to enhance cardiac performance, multilayered tissue ventricle models are required in the future. To that end, FIG inks and their biochemical and structural markers can be further investigated to promote cell infiltration, and to vary local muscle direction, fabricate multilayered tissues and integrate multiple cell types, for example, to achieve vascularization. This work suggests that 3D FIG ink printing will play an important role in promoting standardized and accessible bioprinting processes to recapitulate native organ geometries with microstructural precision.

Online content

Any methods, additional references, Nature Portfolio reporting summaries, source data, extended data, supplementary information, acknowledgements, peer review information; details of author contributions and competing interests; and statements of data and code availability are available at https://doi.org/10.1038/s41563-023-01611-3.

References

1. Frantz, C., Stewart, K. M. & Weaver, V. M. The extracellular matrix at a glance. *J. Cell Sci.* **123**, 4195–4200 (2010).
2. Blazeski, A. et al. Functional properties of engineered heart slices incorporating human induced pluripotent stem cell-derived cardiomyocytes. *Stem Cell Rep.* **12**, 982–995 (2019).
3. LeGrice, I., Pope, A. & Smaill, B. in *Interstitial Fibrosis in Heart Failure* (ed. Villarreal, F. J.) 3–21 (Springer New York, 2005).
4. Ronaldson-Bouchard, K. et al. Advanced maturation of human cardiac tissue grown from pluripotent stem cells. *Nature* **556**, 239–243 (2018).
5. Kleber, A. G. & Rudy, Y. Basic mechanisms of cardiac impulse propagation and associated arrhythmias. *Physiol. Rev.* **84**, 431–488 (2004).
6. Park, S. J. et al. Insights into the pathogenesis of catecholaminergic polymorphic ventricular tachycardia from engineered human heart tissue. *Circulation* **140**, 390–404 (2019).
7. Wang, G. et al. Modeling the mitochondrial cardiomyopathy of barth syndrome with induced pluripotent stem cell and heart-on-chip technologies. *Nat. Med.* **20**, 616–623 (2014).
8. McCain, M. L., Agarwal, A., Nesmith, H. W., Nesmith, A. P. & Parker, K. K. Micromolded gelatin hydrogels for extended culture of engineered cardiac tissues. *Biomaterials* **35**, 5462–5471 (2014).
9. Feinberg, A. W. et al. Muscular thin films for building actuators and powering devices. *Science* **317**, 1366–1370 (2007).
10. Li, R. A. et al. Bioengineering an electro-mechanically functional miniature ventricular heart chamber from human pluripotent stem cells. *Biomaterials* **163**, 116–127 (2018).
11. Karp, J. M. et al. A photolithographic method to create cellular micropatterns. *Biomaterials* **27**, 4755–4764 (2006).
12. Wu, X. et al. Preparation of aligned porous gelatin scaffolds by unidirectional freeze-drying method. *Acta Biomater.* **6**, 1167–1177 (2010).
13. MacQueen, L. A. et al. A tissue-engineered scale model of the heart ventricle. *Nat. Biomed. Eng.* **2**, 930–941 (2018).
14. Capulli, A. K. et al. Jetvalve: rapid manufacturing of biohybrid scaffolds for biomimetic heart valve replacement. *Biomaterials* **133**, 229–241 (2017).
15. Chang, H. et al. Recreating the heart's helical structure-function relationship with focused rotary jet spinning. *Science* **377**, 180–185 (2022).
16. Wang, Z., Lee, S. J., Cheng, H. J., Yoo, J. J. & Atala, A. 3D bioprinted functional and contractile cardiac tissue constructs. *Acta Biomater.* **70**, 48–56 (2018).
17. Yue, K. et al. Synthesis, properties, and biomedical applications of gelatin methacryloyl (GelMA) hydrogels. *Biomaterials* **73**, 254–271 (2015).
18. Lind, J. U. et al. Instrumented cardiac microphysiological devices via multimaterial three-dimensional printing. *Nat. Mater.* **16**, 303–308 (2017).
19. Zhao, Y. et al. A platform for generation of chamber-specific cardiac tissues and disease modeling. *Cell* **176**, 913–927 (2019).
20. Capulli, A. K., MacQueen, L. A., Sheehy, S. P. & Parker, K. K. Fibrous scaffolds for building hearts and heart parts. *Adv. Drug Deliv. Rev.* **96**, 83–102 (2016).
21. Yi, H. G. et al. A bioprinted human-glioblastoma-on-a-chip for the identification of patient-specific responses to chemoradiotherapy. *Nat. Biomed. Eng.* **3**, 509–519 (2019).
22. Daly, A. C., Davidson, M. D. & Burdick, J. A. 3D bioprinting of high cell-density heterogeneous tissue models through spheroid fusion within self-healing hydrogels. *Nat. Commun.* **12**, 753 (2021).
23. Brassard, J. A., Nikolaev, M., Hubscher, T., Hofer, M. & Lutolf, M. P. Recapitulating macro-scale tissue self-organization through organoid bioprinting. *Nat. Mater.* **20**, 22–29 (2021).
24. Jia, W. et al. Direct 3D bioprinting of perfusable vascular constructs using a blend bioink. *Biomaterials* **106**, 58–68 (2016).
25. Ashammakhi, N. et al. Bioinks and bioprinting technologies to make heterogeneous and biomimetic tissue constructs. *Mater. Today Bio* **1**, 100008 (2019).
26. Ouyang, L. et al. Expanding and optimizing 3D bioprinting capabilities using complementary network bioinks. *Sci. Adv.* **6**, abc5529 (2020).
27. Choi, J. R., Yong, K. W., Choi, J. Y. & Cowie, A. C. Recent advances in photo-crosslinkable hydrogels for biomedical applications. *BioTechniques* **66**, 40–53 (2019).
28. Markstedt, K. et al. 3D bioprinting human chondrocytes with nanocellulose-alginate bioink for cartilage tissue engineering applications. *Biomacromolecules* **16**, 1489–1496 (2015).
29. Nadernezhad, A. et al. Nanocomposite bioinks based on agarose and 2D nanosilicates with tunable flow properties and bioactivity for 3D bioprinting. *ACS Appl. Bio Mater.* **2**, 796–806 (2019).
30. Schwab, A. et al. Printability and shape fidelity of bioinks in 3D bioprinting. *Chem. Rev.* **120**, 11028–11055 (2020).
31. Noor, N. et al. 3D printing of personalized thick and perfusable cardiac patches and hearts. *Adv. Sci.* **6**, 1900344 (2019).
32. Kupfer, M. E. et al. In situ expansion, differentiation, and electromechanical coupling of human cardiac muscle in a 3D bioprinted, chambered organoid. *Circ. Res.* **127**, 207–224 (2020).
33. Lee, A. et al. 3D bioprinting of collagen to rebuild components of the human heart. *Science* **365**, 482–487 (2019).
34. Campostrini, G., Windt, L. M., van Meer, B. J., Bellin, M. & Mummery, C. L. Cardiac tissues from stem cells: new routes to maturation and cardiac regeneration. *Circ. Res.* **128**, 775–801 (2021).
35. Ahrens, J. H. et al. Programming cellular alignment in engineered cardiac tissue via bioprinting anisotropic organ building blocks. *Adv. Mater.* **34**, e2200217 (2022).
36. Gladman, A. S., Matsumoto, E. A., Nuzzo, R. G., Mahadevan, L. & Lewis, J. A. Biomimetic 4D printing. *Nat. Mater.* **15**, 413–418 (2016).
37. Siqueira, G. et al. Cellulose nanocrystal inks for 3D printing of textured cellular architectures. *Adv. Funct. Mater.* **27**, 1604619 (2017).

38. Jinkins, K. R., Chan, J., Jacobberger, R. M., Berson, A. & Arnold, M. S. Substrate-wide confined shear alignment of carbon nanotubes for thin film transistors. *Adv. Electron. Mater.* **5**, 1800593 (2018).
39. Caliari, S. R. & Burdick, J. A. A practical guide to hydrogels for cell culture. *Nat. Methods* **13**, 405–414 (2016).
40. Hausmann, M. K. et al. Dynamics of cellulose nanocrystal alignment during 3D printing. *ACS Nano* **12**, 6926–6937 (2018).
41. Pasqualini, F. S., Sheehy, S. P., Agarwal, A., Aratyn-Schaus, Y. & Parker, K. K. Structural phenotyping of stem cell-derived cardiomyocytes. *Stem Cell Rep.* **4**, 340–347 (2015).
42. Bray, M. A., Sheehy, S. P. & Parker, K. K. Sarcomere alignment is regulated by myocyte shape. *Cell Motil. Cytoskeleton* **65**, 641–651 (2008).
43. Kuo, P. L. et al. Myocyte shape regulates lateral registry of sarcomeres and contractility. *Am. J. Pathol.* **181**, 2030–2037 (2012).
44. Geisse, N. A., Sheehy, S. P. & Parker, K. K. Control of myocyte remodeling in vitro with engineered substrates. *Vitr. Cell. Dev. Biol. Anim.* **45**, 343–350 (2009).
45. Grosberg, A. et al. Self-organization of muscle cell structure and function. *PLoS Comput. Biol.* **7**, e1001088 (2011).
46. Bray, M. A. et al. Nuclear morphology and deformation in engineered cardiac myocytes and tissues. *Biomaterials* **31**, 5143–5150 (2010).
47. Lee, H. et al. Cytoskeletal prestress regulates nuclear shape and stiffness in cardiac myocytes. *Exp. Biol. Med.* **240**, 1543–1554 (2015).
48. Carmeliet, E. Conduction in cardiac tissue. Historical reflections. *Physiol. Rep.* **7**, e13860 (2019).
49. Kleber, A. G. & Jin, Q. Coupling between cardiac cells—an important determinant of electrical impulse propagation and arrhythmogenesis. *Biophys. Rev.* **2**, 031301 (2021).
50. Buckberg, G., Hoffman, J. I., Mahajan, A., Saleh, S. & Coghlan, C. Cardiac mechanics revisited: the relationship of cardiac architecture to ventricular function. *Circulation* **118**, 2571–2587 (2008).

Methods

Preparation of gelatin fibre filler

Gelatin fibres were produced by the focused rotary jet spinning method as previously described in more detail[15]. Gelatin (type A, gel strength ~300 g Bloom, Sigma-Aldrich) was dissolved in 1,1,1,3,3,3-hexafuoro-2-propanol (HFIP; Oakwood Chemical, no. 003409) at 5% (w/v). The gelatin/HFIP solution was then injected into a customized spinneret at 1.8 ml min^{-1} using an automated syringe pump (Harvard Apparatus, part no. 703007). The spinneret was rotated at 10,000 r.p.m., extruding the gelatin solution out of three 400 µm holes into long fibre streams that were collected on a rotating collector (Heidolph Hei-Torque Core) at 300 r.p.m. (Supplementary Fig. 1a(i)). The distance from the spinneret to the collector was 15–20 cm, allowing enough time between the spinneret and collection for HFIP evaporation and fibre formation. Fibres were precut to about 1 mm using an array of razor blades and dispersed into anhydrous ethanol at 0.004 g ml^{-1}. The precut fibre solution (40 ml total) was placed in an ice bath and underwent ultrasonication (FB-505, Fisher Scientific) to further fragment the gelatin fibres (Supplementary Fig. 1a(ii)). The length of the gelatin fibres can be controlled by the power amplitude and duration of the sonication. The 13 mg ml^{-1} of gelatin fibres were then crosslinked with a 5:2 molar ratio of *N*,*N*-(3-dimethylaminopropyl)-*N*′-ethyl-carbodiimide hydrochloride (EDC; Sigma-Aldrich) and *N*-hydroxysuccinimide (NHS; Sigma-Aldrich) in anhydrous ethanol for 3 hours while stirring at 260 r.p.m. (Supplementary Fig. 1a(iii)). After the gelatin fibres were washed with water and separated by centrifuge, the fibres were immersed in a solution containing fibronectin protein (50 µg ml^{-1} fibronectin, Corning), 2 µg ml^{-1} EDC (Thermo Fisher Scientific) and 5.5 µg ml^{-1} *N*-hydroxysulfosuccinimide (sulfo-NHS; Thermo Fisher Scientific) diluted in PBS and incubated overnight at 4 °C (Supplementary Fig. 1a(iv)). Fluorescent fibronectin (green fluorescent, HiLyte Fluor 488, Cytoskeleton) was used to confirm the fibronectin coating on the fibres (Supplementary Fig. 1e). The fibres were then washed and centrifuged with deionized water and ×2 concentrated PBS (×2 PBS; Supplementary Fig. 1a(v)–(vi)). The ×2 PBS was made of 16 mM NaH_2PO_4, 272 mM NaCl, 4 mM KH_2PO_4 and 5.2 mM KCl in deionized water. A schematic illustration of the procedure to prepare the fibre fragmentation materials is described in Supplementary Fig. 1a. Fibre length distribution was measured from bright-field images taken by a ×10 EVOS FL microscope, and diameter distribution was measured from confocal microscope (Olympus ix83) images that were captured by a LUCPLFLN-PH ×20 objective (Olympus).

Fabrication of FIG inks and crosslinking process

FIG inks were prepared by mechanically mixing 5–10 wt% prefabricated fibres into a 65 °C prewarmed solution consisting of 2.4 wt% gelatin (type A, gel strength ~175 g Bloom, Sigma-Aldrich) and 2.4 wt% sodium alginate (Sigma-Aldrich) in ×2 PBS (Supplementary Fig. 1a(vii)). After mixing thoroughly, the contents were transferred to a 3 ml syringe and centrifuged at 450*g* for 2 min to remove air bubbles before printing (Supplementary Fig. 1a(viii)). FIG inks were printed using a 3D bio-printer (Bio X, Cellink). The 2D FIG scaffolds were prepared with ~100 µm thickness. After printing, FIG scaffolds were treated with a 1 wt% calcium chloride (Sigma) solution for 5 minutes to crosslink alginate and a 2–8 wt% microbial transglutaminase (Activa TI Transglutaminase, Ajinomoto) solution for 1 hour at room temperature to crosslink the printed FIG scaffolds. The printed scaffold was then treated with 0.1 M ethylenediaminetetraacetic acid disodium salt dihydrate (Sigma-Aldrich) solution for 15 min at room temperature. The Gel–Alg hydrogel inks with 4 wt% gelatin and 4 wt% alginate in the ×2 PBS were used for printing the 3D-printed control models in Figs. 1–3, and Gel–Alg hydrogel inks with both 4 wt% gelatin and 4 wt% alginate, and 2.4 wt% gelatin and 2.4 wt% alginate, in the ×2 PBS were used to compare line printability and cell alignment in Supplementary Figs. 3 and 6a–c, respectively. All post procedures after printing were the same as with the FIG printed scaffolds.

Rheological test of FIG inks

The rheological properties were measured using a Discovery Hybrid 3 Rheometer (TA Instruments). A 0% fibre condition used as a control ink (without fibre) for rheology in Fig. 1e and Supplementary Fig. 2 was prepared with 2.4 wt% gelatin and 2.4 wt% alginate in the ×2 PBS. A 60 mm cone geometry for 0% Gel–Alg inks and a flat plane geometry for FIG inks were used. The plane geometry experimental set-ups used a 500 µm gap height. Viscosity was measured by a shear rate sweep from 0.1 to 1,000 s^{-1} (Supplementary Fig. 2h). An oscillation amplitude sweep was performed by a shear stress sweep from 0.1 to 1,000 Pa at a frequency of 1 Hz (Supplementary Fig. 2b), and the yield stress was evaluated and determined at the crossover point of the storage and loss moduli (Supplementary Fig. 2d). The yield stress for the 0% fibre hydrogel inks could not be quantified using the oscillation amplitude sweep tests as the value ranges were too low. Therefore, the yield stress for the 0% fibre hydrogel inks was calculated using the stress–shear rate graphs (Supplementary Fig. 2c), which showed a plateau region as the shear rate decreased. The cyclic strain test was measured with an oscillatory strain change between 1% and 100% every 1 minute at a frequency of 1 Hz and stress of 0.1 Pa (Supplementary Fig. 2e). All measurements were performed at 25 °C. The temperature sweep test was performed from 10 °C to 40 °C with 2 °C steps at a frequency of 1 Hz and stress of 0.1 Pa (Supplementary Fig. 2f).

3D printing

G-code file, the computational language used to guide 3D printer nozzle pathways, was prepared by slicer software (slic3r), 3D bio-printer (Bio X, Cellink) or hand-script. Gel–Alg hydrogel and FIG scaffolds/patterns were printed onto Petri dishes or gelatin-layer-coated coverslips by a direct-ink-writing method. The gelatin-layer-coated coverslip was used to enhance adhesion between the printed scaffolds and coverslip. It was fabricated by printing a 14 mm by 14 mm mesh square onto coverslips and treating with ultraviolet–ozone for 5 min, using 4 wt% gelatin (type A, gel strength ~175 g Bloom, Sigma-Aldrich) solution. The printing patterns were designed by hand-script G-code, MATLAB (MathWorks) script-generated G-code or 3D bio-printer (Bio X, Cellink). The printing line distance for 2D scaffolds was set to 0.3 mm. STL files of 3D free-standing objects were processed and printed by the 3D bio-printer with a layer height of 0.2 mm for 23 gauge straight nozzles (inner diameter, 0.337 mm) and 0.15 mm for 27 gauge tapered nozzles (inner diameter, 0.21 mm). The G-code for the 3D cone-shaped ventricle chamber was prepared by 3D coordination of a cone shape derived from parabola equations ($y = x^2/(4q)$; q, parameter for shape of parabola: mainly $q = 0.5$ was used; Supplementary Fig. 4a) with a layer height of 0.2 mm using MATLAB. The G-codes were visualized with software (Repetier-Host). The printing condition for the scaffolds was set at a range of 50–100 kPa of printing pressure and 5–20 mm s^{-1} of printing speed with 23 gauge straight or 27 gauge tapered nozzles. The 3D free-standing objects were printed with 70–120 kPa of pressure and 5–10 mm s^{-1} of printing speed using 23 gauge straight nozzles and 27 gauge tapered nozzles at a 6 °C printing bed temperature.

Scaffold structural and biochemical imaging analysis

The gelatin fibre structure in the printed 3D FIG ventricle scaffold was captured by a spinning disc confocal microscope (Olympus ix83) with a UPLSAPO ×10 objective after staining the gelatin fibres using 1 µl ml^{-1} of NHS-Fluorescein (Thermo Fisher Scientific). Fibre alignments were analysed by an ImageJ (National Institutes of Health) plug-in (OrientationJ) with 2° bin size, and the images were colourized based on fibre angle[51]. The colourized images were then processed using a custom MATLAB script to output an OOP value, falling on a normalized scale of 0 (perfectly random) to 1 (perfectly aligned), based on the distribution of reported angles from the OrientationJ-processed image[41]. Scanning electron microscopy images (FESEM Ultra Plus, SmartSEM, ZEISS)

and microcomputed tomography (Xradia Versa 620, ZEISS) images of 3D-printed scaffolds were taken after dehydration using a critical-point dryer (931 GL 2.5, Tousimis). Microcomputed tomography images of 3D structures were imaged by a Versa 620 X-ray microscope (ZEISS) using a microfocus X-ray source (tube voltage of 50 kV and current of 90 μA) and a ×4 objective with wide-field mode at Harvard University's Center for Nanoscale Systems. Some 4,501 projection images were captured per sample on a 16-bit, 2,048 × 2,048, ×4 objective detector with achievable voxel resolutions of 3.19 μm. The 3D data visualization was performed using Dragonfly Pro software.

NRVM and hiPSC-CM cell cultures

NRVMs. The animal protocol numbered 24-01-2 was approved by the Harvard Animal Care and Use Committee and is based on previously published methods[9]. Ventricular tissue was removed from two-day-old Sprague Dawley rats. The tissue was minced by scissors, rinsed in Hank's Balanced Salt Solution (HBSS) and digested in 1 mg ml^{-1} trypsin in HBSS solution at 4 °C for 14 hours overnight. The next day, the tissue was washed in customized media (details in the following) at 37 °C for 4 minutes. The tissue was then further dissociated using 1 mg ml^{-1} collagenase in HBSS solution at 37 °C for 2 minutes. Cells dissociated from the tissue were collected in a prechilled tube containing fresh HBSS without collagenase to quench the digestion. The collagenase step was repeated a total of four times until most of the tissue was digested. The dissociated cells were centrifuged at 250*g* for 8 minutes, resuspended in chilled HBSS and filtered through a 40 μm strainer to remove any remaining bulk tissue. The cells were then centrifuged again at 250*g* for 8 minutes and plated in a T175 flask for 2 hours and 15 minutes to remove the fast-adhering fibroblasts. The non-adhering cells were collected as the primary NRVMs and plated on tissue-engineered scaffolds. Culture media for NRVM were Medium 199 supplemented with 0.01 M HEPES buffer solution, 1% MEM non-essential amino acids, 20 mM glucose, 2 mM L-glutamine, 1.5 μM vitamin B12 and 50 U ml^{-1} penicillin. Some 10% heat-inactivated fetal bovine serum was supplemented to the media for the first two days, and 2% fetal bovine serum supplement was used starting on the third day and changed every other day onward.

The hiPSC-CM culture. The hiPSCs (WTC-11, Coriell Institute, no. GM25256) were seeded onto Geltrex-coated (LDEV-free matrix, Thermo Fisher Scientific) six-well plates and maintained in Essential 8 (E8) medium. At ~60–70% confluency, hiPSCs were passaged using Versene (Life Technologies) into six-well plates for maintenance and twelve-well plates for hiPSC cardiomyocyte differentiation. E8 medium with 5 μM Y-27632 (R&D) was used on the first day of passage. The differentiation process for hiPSC-CMs was conducted for 15 days following published protocols[52]. Differentiation started (day 0) at ~60–70% confluence using 6 μM CHIR909921 (STEMCELL Technologies) with a differentiation medium (RPMI/B27(−)) consisting of RPMI-1640 (Life Technologies) and a B-27 minus insulin supplement after a short rinse with PBS. On day 2, the medium was replaced with the RPMI/B27(−) for 24 hours and changed to the RPMI/B27(−) with 5 μM IWR-1 (STEMCELL Technologies; day 3). After 48 hours of incubation and a quick PBS rinse, the medium was replaced with RPMI/B27(−). On day 7, the medium was replaced with RPMI/B27(−) again. On day 9, cardiomyocyte selection was conducted using 0.4 mM lactate (no. L7022, Sigma-Aldrich) added to the differentiation medium for 48 hours, and 0.4 mM lactate added to RPMI-1680 for the next 48 hours. After cardiomyocyte selection, cells were cultured in the differentiation medium until hiPSC-CM isolation on days 15–17. After visual confirmation of cardiomyocyte contractility (Supplementary Video 2), hiPSC-CMs were isolated after incubating in Accutase (STEMCELL Technologies) for 30 min. Isolated hiPSC-CMs were seeded using STEMdiff Cardiomyocyte Support Medium (STEMCELL Technologies). The culture medium was changed to RPMI/B27(−) every other day.

Cell culture on the printed FIG scaffolds

Before cell seeding, printed scaffolds were sterilized with a 70% ethanol wash for 5 min and ultraviolet–ozone exposure for 4 min. Subsequently, scaffolds were incubated with 50 μg ml^{-1} solution of fibronectin (Corning) in PBS (Gibco, Thermo Fisher Scientific) at 37 °C for 1 h. After the fibronectin solution was washed with PBS, the 2D scaffolds were seeded with 2 M NRVMs and hiPSC-CMs in twelve-well plates. For 3D-printed ventricle chamber seeding, we inserted a printed ventricle scaffold into a polydimethylsiloxane (PDMS) mould made by casting the same 3D-printed ventricle plastic model (VEROCLEAR, Object30, Stratasys). Considering the cells are less likely to be evenly distributed in the 3D structure, NRVMs and hiPSC-CMs were seeded for 3D-printed ventricle models with 5 M and 8 M, and we turned the ventricles upside down after 1 h and 0.5 h, respectively.

Tissue immunostaining and structural analysis

For live/dead cell staining, we cultured NRVMs on fibronectin-coated glass coverslips and FIG scaffolds with 0.5 M cm^{-2} for 96 h. Live/dead-cell-stained images were captured by a confocal microscope (Olympus ix83) with a LUCPLFLNPh ×20 objective after incubating the cells for 5 minutes in 1 μg ml^{-1} Hoechst 33342 in media for live cell staining, and using the ReadyProbes Cell Viability Imaging Kit, Green (~1–2 drops in the 1 ml of media, Thermo Fisher) for dead cell staining. Tissue structure analysis was conducted using confocal microscope immunostaining images of NRVM tissue cultured on the scaffold for 12 days and ventricle for 7–12 days. Washed samples were fixed with 4% (v/v) paraformaldehyde in PBS for 15 min and permeabilized with 0.1% (v/v) Triton-X 100 solution in PBS for 15 min at room temperature. The samples were then incubated in 5% (w/v) bovine serum albumin (BSA) solution in PBS for 30 min at room temperature. Samples were then incubated overnight with 1:100 diluted monoclonal sarcomeric α-actinin (clone EA-53; abcam) or 1:100 Anti-Connexin-43 antibody produced in rabbit (Sigma-Aldrich, no. C-6219) primary antibody in 1 wt% BSA solution at 4 °C. After being washed three times in 0.5 wt% BSA solution for 5 min, the samples were counterstained with 1:200 diluted Alexa Fluor 546-conjugated anti-mouse secondary antibody (Invitrogen, no. A-11003), 1:1,000 diluted Alexa Fluor 633-conjugated phalloidin (Life Technologies, no. A22284) and 1:500 diluted DAPI (Invitrogen) in 1 wt% BSA solution for 2 h at room temperature. After the samples were washed three times with 0.5 wt% BSA solution, they were mounted on the glass to observe immunostaining images using a spinning disc confocal microscope (Olympus ix83). Images were captured by LUCPLFLNPh ×20 and ×40 objectives on a Hamamatsu Orca Flash 4.0 C11440 at 16-bit depth. Background subtraction and *Z*-stack maximum projection were applied for displayed confocal microscope images in figures using ImageJ software. We used ×40 confocal microscope images with 1,024 × 1,024 pixels to quantify nucleus alignment, eccentricity ratio, and sarcomere and F-actin alignments after rotating those images to position the print orientation horizontally. We analysed the angle and length of nuclei in the major and minor axes using an ImageJ plug-in (Analyze particle). We subtracted 90 degrees from the angle results to ensure that the print direction was oriented towards 0 degrees. The eccentricity ratio was calculated by dividing the length of the major axis by the length of the minor axis. Sarcomere and F-actin images were processed with an ImageJ plug-in (OrientationJ) to get colour-coded maps based on cytoskeletal fibre orientation. Based on the distribution of angular orientations, we calculated OOP values that range from zero (random organization) to one (perfect alignment) using custom-made MATLAB (Mathwork) code, as previously published[41].

Optical mapping experiments of cardiac tissues

After observing the spontaneous beating of NRVM tissue at day 3 and iPSC-CM tissue at day 5, we observed Ca^{2+} activities of cardiac tissues on the 3D-printed scaffolds using an optical mapping system at day 5 and day 7, respectively. For hiPSC-CM tissues on the 3D-printed ventricle

scaffolds, we cultured for 14 days before conducting the optical mapping experiment to ensure the structural and functional coupling of the cells in tissues due to the higher number of cells in 3D structures. The optical mapping system includes a modified tandem-lens macroscope (Scimedia) equipped with a high-speed camera (MiCAM Ultima, Scimedia), a Plan APO ×0.63 or ×1 objective (Zeiss), a collimator (Lumencor), a 200 mW mercury lamp (X-Cite exacte, Lumen Dynamics), a high-spatial-resolution scientific complementary metal–oxide semiconductor camera (pco.edge, PCO AG) and 880 nm dark-field light-emitting diode (LED) light. For Ca^{2+} imaging, we used an excitation filter with 580/14 nm, a dichroic mirror with a 593 nm cut-off and an emission filter with 641/75 nm (Semrock). For dark-field imaging, we added a dichroic mirror with a 685 nm cut-off and long-pass emission filter with a 664 nm cut-off filter (Semrock). Cultured tissues were incubated with 2 μM X-Rhod-1 (Invitrogen) for 60 min at 37 °C, rinsed and incubated in dye-free media for an additional 15 min at 37 °C before recording. The recording was conducted in Tyrode's solution (1.8 mM $CaCl_2$, 5 mM glucose, 5 mM HEPES, 1 mM $MgCl_2$, 5.4 mM KCl, 135 mM NaCl and 0.33 mM NaH_2PO_4 in deionized water, pH 7.4, at 37 °C) for NRVM tissue and fresh RPMI/B27(−) for hiPSC-CM tissue. Point stimulation was applied to in vitro cardiac tissues using two platinum electrodes (Sigma-Aldrich) with 1 mm spacing and with 10 V amplitude and 10 ms duration. The platinum electrodes were located at 1.0 mm from the corner of the tissue samples (IonOptix MyoPacer). For each recording, Ca^{2+} and dark-field images were acquired with frame rates of 400 frames per second (f.p.s.) for 10 s. The recording of the top view was performed after the 3D-printed in vitro ventricles moved to the PDMS mould without external stimulation. Post-processing of data was conducted with custom software written in MATLAB (MathWorks) and MiCAM imaging software (MiCAM Ultima, Scimedia). A spatial filter with 3 × 3 pixels was applied to improve the signal-to-noise ratio. The activation time of each pixel was calculated at the average maximum upstroke slope of multiple pulses of X-Rhod-1 signals over a 10 second recording window. Velocity was derived from the difference in activation time that occurred between 1 mm and 5 mm.

MTF analysis and contractile force measurement

FIG MTF chips were manufactured with cantilever designs[53]. G-code was made by hand-script to print FIG ink in the direction of cantilevers; the printing model is shown in Supplementary Fig. 10d, left. MTFs were printed on the coverslip. A cantilever of the MTFs' dimension had a width of 1 mm and a length of 2.5–3 mm. The MTF experiment was performed after 5 days of NRVM culture in a 3.5 mm Petri dish. Video micrographs were recorded on a Zeiss Discovery V12 stereomicroscope with 30 f.p.s. for 5–10 s. The IonOptix MyoPacer was used to apply 1 Hz field electrical stimulation with two parallel platinum electrode wires placed ~3 cm apart. Contractile stress was calculated as previously reported[53]. MTF cantilever images were threshold to binary images. The radius (r) of curvature of each cantilever was calculated using the x projection (blue line in Supplementary Fig. 10d) and original length (white box in Supplementary Fig. 8c). Briefly, numerically approximate r was determined by the following equations:

$$x(r) = \begin{cases} r\sin(L/r), & 2L/\pi < x < L \\ r, & L/2\pi < x < 2L/\pi \end{cases}$$

where L is the original cantilever length and x is the projected length of each cantilever extracted from the cantilever video using ImageJ. The contractile stress σ_c was calculated by applying a modified Stoney's equation:

$$\sigma_c = E{t_{FIG}}^2/6rt_{tissue}(1 + t_{tissue}/t_{FIG})$$

where E is the elastic modulus and t_{FIG} and t_{tissue} are the thicknesses of the FIG scaffolds and tissue, respectively. The average FIG scaffold thickness and tissue thickness for FIG MTFs were ~70 μm and ~10 μm, respectively, and the average PDMS thickness and tissue thickness for PDMS MTFs were 20 μm and 5 μm, respectively. The elastic modulus of FIG was 51 kPa measured by compressing in the fibre direction at 1 Hz oscillation using a dynamic mechanical analyser (DMA1-STAR, Mettler Toledo). The twitch stress was derived by subtracting the peak diastolic stress (minimum stress of contractile stress) from the contractile stresses.

PIV analysis

The hiPSC-CMs were cultured for 15 days in printed 3D FIG ventricle chamber scaffolds. The in vitro model of the heart chamber was moved to the 35 mm Petri dish filled with RPMI/B27(−) with 0.1 μg ml^{-1} of fluorescent beads (green fluorescent microspheres, Cospheric). A 1 Hz field electrical stimulation (IonOptix MyoPacer) was applied with 10–20 V using two parallel platinum electrodes positioned ~30 cm apart. Bead movements were recorded using a stereoscopic microscope (ZEISS Discovery.V12 stereomicroscope) with a HBO 100 fluorescent light source at a ×14 magnification with frame rates of 30 f.p.s. Bright-field images were recorded with a Basler electric ACA2500-14UC USB 3.0 camera at an ×8.5 magnification and 30 f.p.s. with and without 1 Hz field electrical stimulation (spontaneous contraction). Fluorescent image sequences were prepared for analysis using a rolling ball background subtraction (ImageJ) and were analysed by custom software based on the open-source package OpenPIV to reconstruct velocity maps[54]. This resulted in velocity-field profiles as a function of time. These time-dependent velocity profiles were then phase-averaged over the entire cycle to smooth out local fluctuations in performance. For quantitative metrics of cardiac performance, we examined the total mass flux (cardiac output) and ejection fraction resulting from the 3D-printed ventricles as previously reported[15]. Briefly, here we summed the velocity profiles over the basal opening and normalized this value by the fluid density to obtain a 2D instantaneous mass flux with units of grams per metre. Further integrating this 2D value over the basal opening resulted in a 3D estimate of the total mass flux occurring during systole. Finally, knowing this mass flux value, the density of the fluid and the initial starting volume of the ventricle, we could estimate the fraction of fluid ejected during contraction. Based on printing dimensions, a width of 10 mm, height of 10 mm and depth of 11 mm were used to estimate the starting volume, assuming the shape of a half-oblate ellipsoid.

Deformation map analysis of in vitro 3D ventricle models

Deformation mapping was performed as previously reported[15]. Here, in vitro models of the heart chamber were soaked in an RPMI/B27(−) media with 0.1 μg ml^{-1} fluorescent beads for 20–30 minutes to allow the fluorescent beads to adhere to the printed ventricle scaffolds. After the printed in vitro ventricle moved to fresh RPMI/B27(−), beads on the in vitro ventricle were recorded with the same system for PIV data recording. The open-source package OpenPIV (ref. 54) was used to measure displacements in corresponding images by digital image cross-correlation to obtain deformation maps. One frame at the peak diastole was selected as a given reference image, and changes in deformation were measured relative to this frame using OpenPIV. Deformation maps were then normalized by the total ventricle height to produce strain values. To remove null frames and artefacts, images were then masked using a thresholding process (Huang thresholding) with outliers filtered using a rolling kernel density estimate (kernel of size 3 × 3). Here the standard deviation in strain for each kernel was measured, and values that locally exceeded two standard deviations were replaced with mean kernel values.

Statistics and reproducibility

Statistical analysis was conducted to compare cell viability, tissue alignment, nucleus aspect ratio, nucleus angle distribution, tissue

contractility and the Ca^{2+} conduction anisotropy ratio in the longitudinal direction versus the transverse direction between tissues on the printed Gel–Alg hydrogel and the FIG scaffolds. All error bars are given as the standard error of the mean (s.e.m.) unless otherwise noted. Statistical analyses were performed with a two-tailed unpaired Student's *t*-test, assuming unequal variance, a one-way analysis of variance with Tukey post-hoc test within the groups and a two-sample Kolmogorov–Smirnov test, and were conducted unless otherwise noted. *P* values of <0.05 were considered statistically significant. Sample sizes are given for each experimental condition in the figure legends. For representative data and images given in the figures, at least three or more independent experiments were conducted, showing similar results.

Reporting summary

Further information on research design is available in the Nature Portfolio Reporting Summary linked to this article.

Data availability

Data generated or analysed during this study are included in the Article and its Supplementary Information files and publicly available at figshare at https://doi.org/10.6084/m9.figshare.22787714. Additional data may be obtained from the corresponding author upon reasonable request. Source data are provided with this paper.

Code availability

G-code files used in this study are provided in the Supplementary Code. The contractility analysis of in vitro ventricle models was conducted using code from ref. 15 and is available at https://doi.org/10.5281/zenodo.6547775 (ref. 55).

References

51. Rezakhaniha, R. et al. Experimental investigation of collagen waviness and orientation in the arterial adventitia using confocal laser scanning microscopy. *Biomech. Model. Mechanobiol.* **11**, 461–473 (2012).
52. Lian, X. et al. Directed cardiomyocyte differentiation from human pluripotent stem cells by modulating Wnt/β-catenin signaling under fully defined conditions. *Nat. Protoc.* **8**, 162–175 (2013).
53. Al Tanoury, Z. et al. Prednisolone rescues Duchenne muscular dystrophy phenotypes in human pluripotent stem cell–derived skeletal muscle in vitro. *Proc. Natl Acad. Sci. USA* **118**, e2022960118 (2021).
54. Liberzon, A. et al. OpenPIV/openpiv-python: fixed windows conda-forge failure with encoding. Zenodo https://doi.org/10.5281/zenodo.3566451 (2019).
55. SeasDBG. SeasDBG/FRJS: recreating the heart's helical structure-function relationship with focused rotary jet spinning-data analysis (analysis). Zenodo https://doi.org/10.5281/zenodo.6547775 (2022).

Acknowledgements

We thank M. Rosnach for photography and illustrations and A. G. Kleber for discussions regarding cardiac physiology. This work was sponsored by the John A. Paulson School of Engineering and Applied Sciences at Harvard University, the National Science Foundation through the Harvard University Materials Research Science and Engineering Center (DMR-1420570, DMR-2011754 to K.K.P.) and the National Institutes of Health and National Center for Advancing Translational Sciences (UH3HL141798 to W.T.P. and K.K.P.; UG3TR003279 to W.T.P. and K.K.P.) and the National Research Foundation of Korea (NRF) grant funded by the Korea government (MSIT) (RS-2023-00248477, 2022R1A2C2012738 to K.Y.L.). This work was also performed in part at the Harvard University Center for Nanoscale Systems, a member of the National Nanotechnology Coordinated Infrastructure Network, which is supported by the National Science Foundation under award no. ECCS-2025158. Microcomputed tomography imaging reported in this publication was supported by Harvard University, Center for Nanoscale Systems under National Institutes of Health award no. S10OD023519. We gratefully acknowledge financial support by the European Research Council (ERC) under the European Union's Horizon 2020 research and innovation programme (grant agreement no. 810104-PoInt to A.R.B.) and the Deutsche Forschungsgemeinschaft (DFG, German Research Foundation, Project ID No. 201269156—SFB 1032 to A.R.B.). H.A.M.A. thanks the American Chemical Society for support through the Irving S. Sigal Postdoctoral Fellowship. The content is solely the responsibility of the authors and does not necessarily represent the official views of the National Institutes of Health.

Author contributions

K.K.P. supervised the research. S.C., L.A.M. and K.K.P. conceived and designed the study. S.C. developed the fabrication method of the FIG ink, designed and performed 3D printing experiments, analysed data, organized figures and wrote the paper. K.Y.L. performed the optical mapping experiments. H.C. and M.M.P. fabricated the gelatin fibres. K.Y.L., S.L.K., J.F.Z., M.M.P. and A.R.B. analysed data. S.C., S.L.K., Q.J. and H.A.M.A. performed the NRVM harvest with animal protocols. S.C., S.L.K., A.-C.H., X.L. and W.T.P. differentiated hiPSC into cardiomyocytes and cultured hiPSC-CM. R.G. and C.R. assisted in the fabrication of the FIG ink and 3D-printed scaffolds. All authors discussed the results and contributed to the writing of the manuscript.

Competing interests

Harvard College and Sogang University are patent applicants for one pending utility patent, application number 16/756,214, with L.A.M. and K.K.P. included among the inventors. This patent application describes three-dimensional biological tissue formation using macromolecular-fibre-infused additive manufacturing inks. The remaining authors declare no competing interests.

Additional information

Supplementary information The online version contains supplementary material available at https://doi.org/10.1038/s41563-023-01611-3.

Correspondence and requests for materials should be addressed to Kevin Kit Parker.

Peer review information *Nature Materials* thanks Wolfram Zimmermann and the other, anonymous, reviewer(s) for their contribution to the peer review of this work.

nature portfolio

Corresponding author(s): Kevin Kit Parker

Last updated by author(s): May 2, 2023

Reporting Summary

Nature Portfolio wishes to improve the reproducibility of the work that we publish. This form provides structure for consistency and transparency in reporting. For further information on Nature Portfolio policies, see our Editorial Policies and the Editorial Policy Checklist.

Statistics

For all statistical analyses, confirm that the following items are present in the figure legend, table legend, main text, or Methods section.

n/a	Confirmed	
☐	☒	The exact sample size (*n*) for each experimental group/condition, given as a discrete number and unit of measurement
☐	☒	A statement on whether measurements were taken from distinct samples or whether the same sample was measured repeatedly
☐	☒	The statistical test(s) used AND whether they are one- or two-sided *Only common tests should be described solely by name; describe more complex techniques in the Methods section.*
☒	☐	A description of all covariates tested
☒	☐	A description of any assumptions or corrections, such as tests of normality and adjustment for multiple comparisons
☐	☒	A full description of the statistical parameters including central tendency (e.g. means) or other basic estimates (e.g. regression coefficient) AND variation (e.g. standard deviation) or associated estimates of uncertainty (e.g. confidence intervals)
☐	☒	For null hypothesis testing, the test statistic (e.g. *F*, *t*, *r*) with confidence intervals, effect sizes, degrees of freedom and *P* value noted *Give P values as exact values whenever suitable.*
☒	☐	For Bayesian analysis, information on the choice of priors and Markov chain Monte Carlo settings
☒	☐	For hierarchical and complex designs, identification of the appropriate level for tests and full reporting of outcomes
☒	☐	Estimates of effect sizes (e.g. Cohen's *d*, Pearson's *r*), indicating how they were calculated

Our web collection on statistics for biologists contains articles on many of the points above.

Software and code

Policy information about availability of computer code

Data collection	Micro-CT image: Dragonfly Pro version 2022.2.0.1361; Scanning electron microscope: SmartSEM version 05.04.02.00; Rheometer: TA instrument TRIOS version 5.0.0.44608; 3D printer slicer software: Slic3r version 1.3.0 Calcium imaging: MiCAM imaging software version 13.04.20 (BV_Ana, SciMedia);
Data analysis	Statistical analysis conducted using MATLAB 2022 and MIcrosoft Excel 2019 Rheometer: TA instrument TRIOS version 5.0.0.44608; Calcium image analysis : MiCAM imaging software version 13.04.20 (BV_Ana, SciMedia); Contractility analysis of In vitro ventricle models was analyzed by custom made code that are published in Science 377, 180-255 (2022); Orientation order parameter (OOP) analysis was conducted based on the published literature (Stem Cell Reports, (2015), 340-347, 4(3))

For manuscripts utilizing custom algorithms or software that are central to the research but not yet described in published literature, software must be made available to editors and reviewers. We strongly encourage code deposition in a community repository (e.g. GitHub). See the Nature Portfolio guidelines for submitting code & software for further information.

Data

Policy information about availability of data

All manuscripts must include a data availability statement. This statement should provide the following information, where applicable:

- Accession codes, unique identifiers, or web links for publicly available datasets
- A description of any restrictions on data availability
- For clinical datasets or third party data, please ensure that the statement adheres to our policy

All data generated or analysed during this study are included in this published article and available at a Figshare repository.

Human research participants

Policy information about studies involving human research participants and Sex and Gender in Research.

Reporting on sex and gender	The study did not involve human research participants.
Population characteristics	N/A
Recruitment	N/A
Ethics oversight	N/A

Note that full information on the approval of the study protocol must also be provided in the manuscript.

Field-specific reporting

Please select the one below that is the best fit for your research. If you are not sure, read the appropriate sections before making your selection.

☒ Life sciences ☐ Behavioural & social sciences ☐ Ecological, evolutionary & environmental sciences

For a reference copy of the document with all sections, see nature.com/documents/nr-reporting-summary-flat.pdf

Life sciences study design

All studies must disclose on these points even when the disclosure is negative.

Sample size	The determination of our sample size was made to address the effect of fiber alignment on the organization of cardiomyocytes, and we have determined that the selected sample size is sufficient to elucidate the observed effect. Samples sizes are given for each experimental condition in the figure captions (Main Figure 2c, 3b, 4g, Supplementary Figure 1c, 2d, 2i, 5c, 6c, 6g, 7, 8b, 10f, 11c-d, 11e)
Data exclusions	No data were excluded from the analyses.
Replication	All experiments were performed three to six times independently, showing similar results.
Randomization	No specific randomization method was used. Samples were processed and allocated according to specific experimental conditions and treatments.
Blinding	All data analysis were subjected to the same automated data processing, thus blind-test would not affect the result.

Reporting for specific materials, systems and methods

We require information from authors about some types of materials, experimental systems and methods used in many studies. Here, indicate whether each material, system or method listed is relevant to your study. If you are not sure if a list item applies to your research, read the appropriate section before selecting a response.

Materials & experimental systems

n/a	Involved in the study
☐	☒ Antibodies
☐	☒ Eukaryotic cell lines
☒	☐ Palaeontology and archaeology
☐	☒ Animals and other organisms
☒	☐ Clinical data
☒	☐ Dual use research of concern

Methods

n/a	Involved in the study
☒	☐ ChIP-seq
☒	☐ Flow cytometry
☒	☐ MRI-based neuroimaging

Antibodies

Antibodies used

Mouse monoclonal [EA-53] anti Sarcomeric Alpha Actinin, abcam, ab9465 (1:100).
Anti-Connexin-43 antibody produced in rabbit ,Sigma-Aldrich, C-6219 (1:100)
goat anti-Mouse IgG (H+L) Highly Cross-Adsorbed Secondary Antibody, Alexa Fluor Plus 546, Invitrogen, A-11003 (1:300)
Alexa Fluor 633-conjugated Phalloidin (Invitrogen, A22284) (1:1000)

Validation

All antibodies used in this study are commercially available and validated for the species and assay used as described on the manufacturer's web page

Eukaryotic cell lines

Policy information about cell lines and Sex and Gender in Research

Cell line source(s)

Neonatal rat ventricular myocytes (NRVMs) with mixed genders were isolated from two-day-old neonatal neonatal CRL: CD (Sprague-Dawley, SD) using published methods. Human induced pluripotent stem cells were acquired commercially (WTC11, Coriell Institue, cat# GM25256). The cell lines are available through Coriell at https://www.coriell.org/

Authentication

Cell viability, sterility, and behavior of human pluripotent stem cell were authenticated by the vendor (Coriell Institue) using qRT-PCR, STR profiling, immunostaining and flow cytometric detection (SSEA4), karyotyping.

Mycoplasma contamination

Cells tested negative for mycoplasma contamination as specified by the provider.

Commonly misidentified lines
(See ICLAC register)

No commonly misidentified lines were used in this study.

Animals and other research organisms

Policy information about studies involving animals; ARRIVE guidelines recommended for reporting animal research, and Sex and Gender in Research

Laboratory animals

Neonatal rat ventricular myocytes were isolated from 2-day old Sprague-Dawley using published methods.

Wild animals

The study did not involve wild animals.

Reporting on sex

N/A

Field-collected samples

The study did not involve samples collected from the field.

Ethics oversight

All procedures were approved by the Harvard Animal Care and Use Committee (protocol number: 24-01-2).

Note that full information on the approval of the study protocol must also be provided in the manuscript.